

Joint H α and X-Ray Observations of Massive X-Ray Binaries. II. The Be X-ray Binary and Microquasar LS I +61 303

E. D. Grundstrom, S. M. Caballero-Nieves, D. R. Gies¹,
W. Huang^{1,2}, M. V. McSwain^{1,3,4}, S. E. Rafter, R. L. Riddle^{1,5},
S. J. Williams, and D. W. Wingert¹

*Center for High Angular Resolution Astronomy and
Department of Physics and Astronomy,*

Georgia State University, P. O. Box 4106, Atlanta, GA 30302-4106;

*erika@chara.gsu.edu, scaballero@chara.gsu.edu, gies@chara.gsu.edu, wenjin@astro.caltech.edu,
mcswain@astro.yale.edu, rafter@chara.gsu.edu, riddle@tmt.org, swilliams@chara.gsu.edu,
wingert@chara.gsu.edu*

ABSTRACT

We present the results of an H α monitoring campaign on the BeXRB and microquasar system LS I +61 303. We use radial velocity measurements of He I lines in our spectra to re-evaluate the orbital elements and to better establish the time of periastron. We list equivalent widths and other parameters for the H α emission line and discuss the orbital phase related variations observed. We call attention to a dramatic episode of emission weakening that occurred in less than a day that probably resulted from exposure to a transient source of ionizing radiation. We argue that the increase in H α and X-ray emission following periastron probably results from the creation of an extended density wave in the disk created by tidal forces. We also discuss estimates of the size of the disk from the H α equivalent width measurements, and we suggest that the disk radius from the average equivalent width corresponds to a resonant truncation radius of the disk while the maximum equivalent width corresponds to a radius limited by the separation of the stars at periastron. We note that a nearby faint companion is probably an unrelated foreground object.

Subject headings: binaries: spectroscopic — stars: early-type — stars: emission-line, Be — stars: individual (LS I +61 303) — stars: neutron — stars: winds, outflows

1. Introduction

The remarkable binary system LS I +61 303 is one of the best studied microquasars in the

¹Visiting Astronomer, Kitt Peak National Observatory, National Optical Astronomy Observatory, operated by the Association of Universities for Research in Astronomy, Inc., under contract with the National Science Foundation.

²Current address: Department of Astronomy, California Institute of Technology, MS 105-24, Pasadena, CA 91125

³Current Address: Astronomy Department, Yale University, New Haven, CT 06520-8101

⁴NSF Astronomy and Astrophysics Postdoctoral Fellow

⁵Current Address: Thirty Meter Telescope, 2632 E. Washington Blvd., Pasadena, CA 91107

sky (Massi 2004). It consists of a rapidly rotating Be star surrounded by a dense circumstellar disk and a compact companion that is a source of both orbital phase modulated X-ray (Paredes et al. 1997; Leahy 2001; Wen et al. 2006) and radio flux (Taylor et al. 1992; Gregory 2002). High angular resolution observations suggest that the system has precessing, relativistic radio jets (Massi et al. 2004), and these jets may be the source of variable and very high energy, γ -ray emission (Albert et al. 2006). The companion is generally considered to be a magnetic neutron star, but it may be a black hole (Punsly 1999). The orbital parameters were recently reanalyzed by Casares et al. (2005)

who confirmed the high eccentricity of the system and discussed the possible mass range. Their work shows that the orbital phases of the X-ray and radio maxima do not occur at periastron but are curiously delayed by a significant fraction of the orbital period. The disk that feeds the companion is a strong source of $H\alpha$ emission, and there is a well established record of the emission line variations over the past decade (Paredes et al. 1994; Zamanov et al. 1999; Liu et al. 2000; Zamanov et al. 2001; Liu & Yan 2005). Zamanov et al. (1999) demonstrated that some of the emission line properties vary with the orbital period, presumably as the result of the companion’s varying gravitational pull.

Here we present the results of a new observational effort on the $H\alpha$ variations in LS I +61 303 that we launched to investigate the co-variations with the X-ray flux as recorded by the All-Sky Monitor (ASM) instrument aboard the *Rossi X-ray Timing Explorer (RXTE)* satellite. It follows similar investigations of Cyg X-1 (Gies et al. 2003), LS I +65 010 (Grundstrom et al. 2006a), and HDE 245770 = A 0535+26 and X Per (Grundstrom et al. 2006b). We first describe radial velocity measurements and a re-evaluation of the orbital elements in §2. Then we turn in §3 to the temporal variations observed in the $H\alpha$ profile on rapid, orbital, and long term timescales. We discuss the results in the context of the disk truncation model of Okazaki et al. (2002) in §4.

2. Radial Velocities and Orbital Elements

We obtained a set of 100 spectra of LS I +61 303 between 1998 August and 2000 December. The observations were made with the Kitt Peak National Observatory 0.9 m coudé feed telescope during six runs. We used two spectrograph arrangements to record the red spectral region around $H\alpha$ with resolving powers of $R = \lambda/\Delta\lambda = 4100$ and 9500. The details about the spectra and their reduction are given in a companion paper on LS I +65 010 (Grundstrom et al. 2006a). We also recorded the spectrum of a nearby visual companion, and we discuss its properties in the Appendix.

All the spectra record the $H\alpha$ emission line and the He I $\lambda 6678$ feature. The He I $\lambda 6678$ line appears in most spectra as a weak and narrow absorption core flanked by emission wings (see Fig. 2

below). We suspect that this line is a composite of a partial photospheric absorption line with wing emission and central absorption that originates in the inner disk. We assume that the radial velocity variations of this composite profile represent the motion of the Be star since the line formation probably occurs very close to the photosphere of the Be star. We note in passing that the half-width at half-minimum in the absorption core of He I $\lambda 6678$ is 101 km s^{-1} in most of our spectra. This is similar to the projected rotational velocity $V \sin i = 113 \text{ km s}^{-1}$ reported by Casares et al. (2005), but much smaller than that found earlier by Hutchings & Crampton (1981) of $V \sin i = 360 \pm 25 \text{ km s}^{-1}$. This suggests that some of the blue spectral lines measured by Casares et al. (2005) may also have been affected by weak emission in the line wings that made the absorption cores appear more narrow.

We measured radial velocities by cross-correlating each spectrum with a template spectrum formed from the average of 24 spectra from our run in 2000 December. The cross-correlation was made over the spectral region in the immediate vicinity of He I $\lambda 6678$, although we also included the region surrounding He I $\lambda 7065$ for the spectra from the 2000 October and December runs that also recorded this line. These relative velocities were transformed to an absolute scale by adding the radial velocity of the template spectrum, -43.1 km s^{-1} , found by parabolic fitting of the cores of He I $\lambda\lambda 6678, 7065$. We also obtained cross-correlation velocities of the interstellar line at 6613 \AA to monitor the radial velocity stability of our measurements. All these results are reported in Table 1 (given in full in the electronic edition) that lists the heliocentric Julian date of mid-exposure, orbital phase, radial velocity, observed minus calculated residual from the fit, and the interstellar line offset (plus columns describing the $H\alpha$ profile discussed in §3). The typical measurement error is $\pm 2.1 \text{ km s}^{-1}$ based upon the scatter between pairs of observations at closely spaced times.

Many recent papers on the orbital properties of LS I +61 303 adopt an arbitrary zero-phase at HJD 2,443,366.775 (Taylor & Gregory 1982) and an orbital period of $26.4960 \pm 0.0028 \text{ d}$, which was determined by Gregory (2002) from a careful study of the radio flux curve. Here we adopt the same convention for orbital phase that we denote

by $\phi(\text{TG})$.

We determined orbital elements using the non-linear, least-squares program of Morbey & Brosterhus (1974). We also included the radial velocity data from the recent study by Casares et al. (2005), but we found that our velocities are systematically lower than theirs by -9.4 km s^{-1} so we added this value to their measurements for ease of comparison. Our first fit using all the available velocities is shown as the dotted line in Figure 1, and the resulting orbital elements are listed in column 4 of Table 2. The r.m.s. of this fit is 10.4 km s^{-1} , which is about five times larger than the estimated measurement error. This large scatter is caused by temporal changes in the shape of the He I $\lambda 6678$ profile. For example, the six very low velocity measurements shown in Figure 1 were made during a remarkable episode of reduced H α emission strength (§3) when the He I emission wings disappeared and the absorption core became broader. Thus, we selectively zero-weighted these six measurements and five other very discrepant points that also appeared to display profile shape changes. The fit resulting from this edited set of velocities is shown as a solid line in Figure 1, and the corresponding orbital elements are given in column 5 of Table 2.

Our results are generally in good agreement with earlier determinations of the elements by Hutchings & Crampton (1981) and Casares et al. (2005) (given in columns 2 and 3 of Table 2, respectively). The largest range in results is found for the orbital eccentricity e , and unfortunately the paucity of measurements in the orbital phase range $0.4 - 0.5$ limits the accuracy of the estimate in our work. Our final result of $e = 0.55 \pm 0.05$ is somewhat lower than the estimate of $e = 0.8 \pm 0.1$ from fits of the IR light curve (Martí & Paredes 1995). Models for the accretion flux variations indicate an eccentricity in the range $e = 0.3$ (Leahy 2001) to $e = 0.6$ (Taylor et al. 1992). Periastron occurs at phase $\phi(\text{TG}) = 0.301 \pm 0.011$. This is in reasonable agreement with the expectation from the radio model of Gregory (2002) that places the phase of periastron in the range $\phi(\text{TG}) = 0.33 - 0.40$.

3. H α Variations

The H α emission line is formed in the circumstellar disk of the Be star, and here we examine the temporal variations in the profile to investigate how the changes in the disk are related to changes in the accretion flux from the vicinity of the companion. The H α profile appears as a double-peaked emission line in most of our spectra, and we made a number of measurements to characterize the shape and strength of the emission. These measurements are summarized in Table 1. Column 6 of Table 1 lists the numerical integration of the line flux that includes the full extent of the line wings. Since the emitting gas in the disk probably experiences Keplerian rotation (Porter & Rivinius 2003), the high velocity wings are formed closest to the Be star. We measured the radial velocity of the wings based upon a bisector position determined using the method of Shafter, Szkody, & Thorstensen (1986). This method samples the line wings using oppositely signed Gaussian functions and determines the mid-point position between the wings by cross-correlating these Gaussians with the profile. We used Gaussian functions with $\text{FWHM} = 200 \text{ km s}^{-1}$ at sample positions in the wings of $\pm 390 \text{ km s}^{-1}$, and these radial velocities are given in column 7 of Table 1. Zamanov et al. (1999) advocated making fits of the double-peaked H α profile using Gaussian functions to match the violet V and red R peaks, and we have followed their approach for consistency. These double-Gaussian fits were restricted to the inner part of the profile ($|\Delta\lambda| < 7 \text{ \AA}$) since the wings are much more extended than those of Gaussian functions. The remaining columns in Table 1 list the parameters for these fits: radial velocity of the V peak (col. 8), radial velocity of the R peak (col. 9), ratio of the equivalent widths of the V and R components (col. 10), V/R peak intensity ratio (col. 11), FWHM for the V peak (col. 12), and FWHM for the R peak (col. 13).

We find evidence for temporal variations on timescales of days and longer. The most dramatic change in the H α profile that we observed occurred in 1999 October. During the first three nights of this run the H α profile appeared at normal strength (top plot in Fig. 2), but in the course of 24 hours or less the emission strength declined by about a factor of ten (lower plot in Fig. 2). The

equivalent width over the next two days stayed at record low values relative to existing measurements (Paredes et al. 1994; Zamanov et al. 1999; Liu et al. 2000; Zamanov et al. 2001; Liu & Yan 2005). At the same time the emission in the wings of He I $\lambda 6678$ also disappeared revealing a broader photospheric line. Liu & Yan (2005) obtained a spectrum six days after our last weak emission observation, and by that time the emission equivalent width was back to normal levels. We measured a projected rotational velocity for the weak emission spectra of $V \sin i = 104 \pm 5 \text{ km s}^{-1}$ from a comparison of the width of He I $\lambda 6678$ with that in model profiles (Lanz & Hubeny 2003) convolved with a rotational broadening function. This is close to the value obtained by Casares et al. (2005), but we caution that this is probably only a lower limit since the He I profile (like H α) is still probably affected by emission components even during this weak emission phase.

It is hard to imagine any process that would change the density properties of the Be star's disk so significantly in such a short time span. We suggest instead that the neutral hydrogen in the disk was almost totally ionized at that time by exposure to energetic radiation from the vicinity of the companion. We show in Figure 3 the contemporary variations of the radio flux as observed with the NRAO Green Bank Interferometer⁶ (Ray et al. 1997), the daily averaged 5 – 12 keV X-ray flux observed with *RXTE*/ASM⁷ (Levine et al. 1996), and the H α equivalent width. Although there is no evidence of any X-ray flare at that time, a secondary radio brightening did occur about the time of the H α decline. However, since the H α strength appeared relatively normal during other radio bursts, it is not clear how or if this secondary maximum is related to the H α weakening event. If the radio emission forms in the relativistic jets, then it is possible that the secondary radio maximum originated at positions further away from the orbital plane where the inner Be star disk was more directly illuminated by jet emission. We note that the emission weakening event occurred near apastron, an orbital phase where Liu & Yan (2005) also observed rapid variations in the H α profile.

We next turn to H α variations related to the or-

⁶<ftp://ftp.gb.nrao.edu/pub/fghigo/gbdata/gdata/00README>

⁷<http://xte.mit.edu>

bital period. Zamanov et al. (1999) demonstrated that the variations in the relative strengths of the V and R peaks are least partially related to orbital phase (see their Fig. 3), and our results appear to support their conclusion. We show in the lower panel of Figure 4 the ratio of the equivalent widths of the V and R fitted components (Table 1) plotted as a function of the orbital phase. We see that the V peak appears to strengthen relative to the R peak around periastron, $\phi(\text{TG}) = 0.30$. This strengthening of the short wavelength side of the profile also appears to shift the wing radial velocity to lower values. The top panel of Figure 4 shows how the wing velocity attains a minimum near periastron with a velocity curve that is markedly different from the orbital one (shown as a dotted line). The middle panel shows the average radial velocity of the V and R peaks that show no evidence of orbital motion.

We compare in Figure 5 the H α equivalent width variations with orbital phase to those observed in the radio and X-ray fluxes. The lower panel shows our equivalent width measurements combined with 159 other published measurements (Paredes et al. 1994; Zamanov et al. 1999; Liu et al. 2000; Zamanov et al. 2001; Liu & Yan 2005) that we have binned into ten phase groups (after omitting the six unusually low measurements from the 1999 October decline). We see that when averaged over many cycles there appears to be a coherent cyclic variation in emission strength that attains a maximum near $\phi(\text{TG}) = 0.55$. A similar kind of variation is seen in the orbital phase binned X-ray fluxes from *RXTE*/ASM (Paredes et al. 1997; Leahy 2001). The top panel of Figure 5 shows the binned radio curve from the Green Bank Interferometer. Note that the radio brightenings from cycle to cycle show significant variation in the shape of the light curve and phase of maximum (Gregory 2002).

Finally we show in Figure 6 these same three fluxes over the period of active observation. The top panel shows the Green Bank Interferometer flux density observations at 2.25 GHz that we averaged by binning into time intervals equal to three orbital periods (bins of 79.5 d), and the middle panel illustrates the *RXTE*/ASM X-ray fluxes binned in the same way. The lower panel shows the individual H α equivalent widths from our measurements (*plus signs*) and from other published

measurements (*X signs*). Gregory (2002) reported evidence of a long (1167 d) periodicity in the radio measurements, and Zamanov & Martí (2000) showed that a comparable timescale is found in the H α properties. There are two maxima visible that are separated by about 1200 d in the H α time series, but the coverage is too sparse to verify whether other cyclic maxima are present.

4. Discussion

The circumstellar disks of the BeXRBs are comparable in many ways to those of other Be stars, but their outer radii are probably limited by the gravitational influence of their compact companions (Zamanov et al. 2001). Reig, Fabregat, & Coe (1997) show that the maximum H α emission equivalent widths (a good measure of the maximum disk size) are correlated with orbital period for the BeXRBs. Okazaki & Negueruela (2001) found that these limiting radii are defined by the closest approach of the companion in the high eccentricity systems and by resonances between the orbital period and the disk gas rotational periods in the low eccentricity systems. LS I +61 303 has an orbital eccentricity that falls between these two cases, where the important resonance radii are comparable in size to the periastron separation.

We can estimate the disk radius for LS I +61 303 from the H α equivalent width data shown in Figure 6. We recently presented numerical models of the circumstellar disks of Be stars (Grundstrom & Gies 2006), and we demonstrated that there are monotonic relationships between the emission line equivalent width and the ratio of the angular half-width at half maximum emission of the projected disk major axis to the radius of the star. The relationship depends upon the temperature of the star, the inclination of the disk normal to the line of sight, and the adopted outer boundary for the disk radius. We assumed a primary star effective temperature of $T_{\text{eff}} = 29850$ K appropriate to a B0 V classification (Harmanec 1988), although we note that a lower temperature may be possible (Howarth 1983). Figure 7 illustrates the relations for the inclination limits of $i = 10^\circ$ and $i = 60^\circ$ suggested by Casares et al. (2005), and we use the mean of these cases in the radius estimations. Note that Hutchings & Crampton (1981) argue that the inclination may be larger,

and if so, then our radius estimates will be somewhat low. We adopted an outer boundary for the disk as the Roche radius of the primary star at apastron. This assumption is not critical to the radius estimate since only weak, optically thin emission originates in the outer parts of the disk model.

The mean H α equivalent width from the data presented in Figure 6 (less the very low points from 1999 October) is $W_\lambda = -11.7 \pm 2.5$ Å (standard deviation), and from the relations shown in Figure 7 the corresponding ratio of disk to stellar radius is $R_d/R_s = 4.6 \pm 0.4$. The expected disk truncation radius due to resonances with the orbital motion is given by

$$\begin{aligned} \frac{R_n}{R_s} &= \left(\frac{GM_s}{4\pi^2} \right)^{1/3} \frac{1}{R_s} \left(\frac{P_{\text{orbit}}}{n} \right)^{2/3} \quad (1) \\ &= 37.4 \frac{(M_s/M_\odot)^{1/3}}{R_s/R_\odot} \frac{1}{n^{2/3}} \quad (2) \end{aligned}$$

where n is the integer number of disk gas rotational periods per one orbital period. Okazaki & Negueruela (2001) predict that the $n = 4$ truncation radius will dominate in moderate eccentricity systems, and assuming a stellar mass of $M_s/M_\odot = 12.5 \pm 2.5$ (Casares et al. 2005) and a radius of $R_s/R_\odot = 6.7 \pm 0.9$ from the spectral classification (Harmanec 1988), then the predicted $n = 4$ truncation radius is $R_d/R_s = 5.1 \pm 0.8$. This agrees within errors with the estimate from the mean equivalent width given above, so that the observations are consistent with the idea that the disk radius is regulated by the $n = 4$ resonance. Note that Casares et al. (2005) suggest that the disk contributes about 35% of the total continuum flux, so that the disk to stellar continuum flux ratio is $\epsilon = 0.54$ in the optical. If so, then we need to rescale the equivalent width by a factor of $1 + \epsilon$ in order to scale the H α emission flux to the stellar flux alone. This leads to an estimated disk radius of $R_d/R_s = 5.5 \pm 0.5$ (see Fig. 7), which is slightly larger than the $n = 4$ truncation radius.

The record of H α emission measurements indicates that the disk may occasionally grow to an even larger radius. The two equivalent width maxima shown in Figure 6 reach $W_\lambda = -18.5 \pm 0.5$ Å, and this value corresponds to a disk radius of $R_d/R_s = 5.6 \pm 0.1$ (for $\epsilon = 0$). The separation of

the stars at periastron is given by

$$\frac{R_p}{R_s} = \frac{(1-e)a}{R_s} = 16.8 \frac{(M_{\text{total}}/M_{\odot})^{1/3}}{R_s/R_{\odot}} \quad (3)$$

and this is equal to 6.1 ± 1.2 for $M_{\text{total}} = (14.5 \pm 4.0)M_{\odot}$ (Casares et al. 2005). Thus, it appears that the times of the largest observed H α emission correspond to epochs when the disk almost reaches the limiting radius set by the close passage of the companion at periastron.

Okazaki et al. (2002) have made numerical hydrodynamical simulations of the Be star's disk response to the gravitational influence of a compact companion in an elliptical orbit. They show that the tidal pulls at periastron lead to the development of a large spiral wave in the disk that can extend far beyond the truncation radius and out to the vicinity of the companion (see their Fig. 11). Furthermore, Hayasaki & Okazaki (2005) show that a similar spiral pattern can be induced in the accretion disk surrounding the companion in the times shortly after periastron and that the presence of the pattern can promote mass accretion. We speculate that processes like these are probably at work in LS I +61 303. The simulations show that the spiral wave starts at periastron as a density enhancement in the part of the disk facing the companion. The longitude of periastron is $\omega = 57^\circ$, so the portion of the disk facing the companion at periastron will have a negative radial velocity for our line of sight, and the fact that we observe an increase in the strength of the approaching V peak of H α at periastron (Fig. 4) is consistent with the formation of a spiral wave enhancement then. As the spiral feature develops after periastron, disk gas would be carried outwards past the truncation radius, and the mass accretion processes would then begin in earnest. The geometrical extension of the disk after periastron associated with the spiral feature would probably increase the projected area on the sky of high H α optical depth causing the emission feature to increase in strength as observed (Fig. 5).

Our new determination of the time of periastron confirms that the X-ray and radio flux maxima occur some time after periastron (Massi 2004). Figure 5 shows that the X-ray flux attains a maximum near orbital phase $\phi(\text{TG}) = 0.5$ while the radio maximum occurs later near $\phi(\text{TG}) = 0.7$. If the mass transfer process were instantaneous, we

might expect that both fluxes would peak at periastron where the companion encounters the densest part of the disk. However, Taylor et al. (1992) and Martí & Paredes (1995) argue that if the process can be described by Bondi-Hoyle accretion then the mass accretion rate will also depend on the relative gas and accretor velocity and a second peak will occur later near apastron where the accretor's orbital velocity is slower. Massi (2004) suggests that the first X-ray peak corresponds to the periastron accretion increase (with a phase lag caused by inverse Compton losses of relativistic electrons due to the large stellar flux field) and that the second radio peak occurs near the slow motion apastron phase (where Compton losses are reduced because the stellar flux is weaker). If this radio flux peak arises from jets, then it is possible that ionizing radiation from the jets will lower the neutral H population and H α emission (leading to an H α minimum near apastron; see Fig. 5). We speculate that the ionizing flux may sometimes become quite strong (perhaps from knots that develop in the jets) and cause sudden decreases in H α emission strength such as we observed in 1999 October (Fig. 3).

Our study indicates that the extent and shape of the Be star's disk has a significant influence on the mass transfer rate in this microquasar system. We show in the next paper in this series that similar limiting disk radii and spiral wave extensions are also found in the BeXRB systems HDE 245770 and X Per.

We thank Daryl Willmarth and the staff of KPNO for their assistance in making these observations possible. The X-ray results were provided by the ASM/RXTE teams at MIT and at the RXTE SOF and GOF at NASA's GSFC. The Green Bank Interferometer is a facility of the National Science Foundation operated by the NRAO in support of NASA High Energy Astrophysics programs. This work was supported by the National Science Foundation under grants AST-0205297, AST-0506573, and AST-0606861. Institutional support has been provided from the GSU College of Arts and Sciences and from the Research Program Enhancement fund of the Board of Regents of the University System of Georgia, administered through the GSU Office of the Vice President for Research.

A. Visual Companion

LS I +61 303 has a nearby visual companion that we also recorded in the spectra made in 2000 December. This companion star has a separation of $11''.2$ and a position angle of 167° from LS I +61 303 according to coordinates listed in the Guide Star Catalog II⁸ (where the companion is designated 0404701738). The companion is approximately 3.5 mag fainter in the optical than LS I +61 303. Our average spectrum shows a very broad H α absorption line, no He I $\lambda 6678$, a few weak metallic lines, and an interstellar line at 6613 Å that is identical in appearance to its counterpart in the spectrum of LS I +61 303. We compared the spectrum to several in the atlas by Valdes et al. (2004), and we tentatively classify the star as type A2 V. The radial velocity of the star from the H α line is -40 ± 2 km s⁻¹.

It is possible that this companion is an outlying member of the Cas OB6 association as is LS I +61 303 (Mirabel, Rodrigues, & Liu 2004). The companion's radial velocity is comparable to that of other association members (Hillwig et al. 2006) including the nearby multiple star HD 16429 (McSwain 2003), and the similarity of the interstellar line strengths suggests a distance comparable to that of LS I +61 303. However, the companion also appears in the 2MASS All-Sky Catalog of Point Sources (Cutri et al. 2003) (with a designation of 2MASS 02403208+6113340), and the near-IR magnitudes suggest that the star is closer than Cas OB6. Suppose the absolute K -band magnitude for a A2 V star is $M_K = 1.2 \pm 0.6$ (Cox 2000) and that the extinction is $A(K) = 0.36E(B-V) = 0.3$ (Howarth 1983; Fitzpatrick 1999). Then for the 2MASS magnitude of $K = 11.55 \pm 0.02$, the estimated distance is 1.0 ± 0.4 kpc, which would place the star in the foreground of the Cas OB6 stars at a distance of 1.9 kpc (Hillwig et al. 2006). Thus, unless the 2MASS magnitudes and/or the spectroscopic estimate of absolute magnitude are wrong, this companion is probably a chance optical alignment rather than a neighbor of LS I +61 303.

⁸<http://vizier.u-strasbg.fr/cgi-bin/VizieR?-source=I/271>

REFERENCES

- Albert, J., et al. 2006, *Science*, 312, 1771
- Casares, J., Ribas, I., Paredes, J. M., Martí, J., & Allende Prieto, C. 2005, *MNRAS*, 360, 1105
- Coe, M. J. 2000, in *The Be Phenomenon in Early-Type Stars*, IAU Coll. 175 (ASP Conf. Vol. 214), ed. M. A. Smith, H. F. Henrichs, & J. Fabregat (San Francisco: ASP), 656
- Cox, A. N. (ed.) 2000, *Allen's Astrophysical Quantities* (4th Ed.) (New York: AIP/Springer-Verlag)
- Cutri, R. M., et al. 2003, *The 2MASS All-Sky Catalog of Point Sources* (Pasadena: Univ. Massachusetts/IPAC)
- Fitzpatrick, E. L. 1999, *PASP*, 111, 63
- Gies, D. R., et al. 2003, *ApJ*, 583, 424
- Gregory, P. C. 2002, *ApJ*, 575, 427
- Grundstrom, E. D., & Gies, D. R. 2006, *ApJ*, in press
- Grundstrom, E. D., et al. 2006a, *ApJ*, submitted
- Grundstrom, E. D., et al. 2006b, *ApJ*, submitted
- Harmanec, P. 1988, *Bull. Astr. Inst. Cz.*, 39, 329
- Hayasaki, K., & Okazaki, A. T. 2005, *MNRAS*, 360, L15
- Hillwig, T. C., Gies, D. R., Bagnuolo, W. G., Jr., Huang, W., McSwain, M. V., & Wingert, D. W. 2006, *ApJ*, 639, 1069
- Howarth, I. D. 1983, *MNRAS*, 203, 801
- Hutchings, J. B., & Crampton, D. 1981, *PASP*, 93, 486
- Lanz, T., & Hubeny, I. 2003, *ApJS*, 146, 417
- Leahy, D. A. 2001, *A&A*, 380, 516
- Levine, A. M., Bradt, H., Cui, W., Jernigan, J. G., Morgan, E. H., Remillard, R., Shirey, R. E., & Smith, D. A. 1996, *ApJ*, 469, L33
- Liu, Q. Z., Hang, H. R., Wu, G. J., Chang, J., & Zhu, Z. X. 2000, *A&A*, 359, 646
- Liu, Q. Z., & Yan, J. Z. 2005, *New Astr.*, 11, 130
- Massi, M. 2004, *A&A*, 422, 267
- Massi, M., Ribó, M., Paredes, J. M., Garrington, S. T., Peracaula, M., & Martí, J. 2004, *A&A*, 414, L1
- Martí, J., & Paredes, J. M. 1995, *A&A*, 298, 151
- McSwain, M. V. 2003, *ApJ*, 595, 1124
- McSwain, M. V., Gies, D. R., Huang, W., Wiita, P. J., Wingert, D. W., & Kaper, L. 2004, *ApJ*, 600, 927
- Mirabel, I. F., Rodrigues, I., & Liu, Q. Z. 2004, *A&A*, 422, L29
- Morbey, C., & Brosterhus, E. B. 1974, *PASP*, 86, 455
- Okazaki, A. T., Bate, M. R., Ogilvie, G. I., & Pringle, J. E. 2002, *MNRAS*, 337, 967
- Okazaki, A. T., & Negueruela, I. 2001, *A&A*, 377, 161
- Paredes, J. M., Martí, J., Peracaula, M., & Ribo, M. 1997, *A&A*, 320, L25
- Paredes, J. M., et al. 1994, *A&A*, 288, 519
- Porter, J. M., & Rivinius, Th. 2003, *PASP*, 115, 1153
- Punsly, B. 1999, *ApJ*, 519, 336
- Ray, P. S., et al. 1997, *ApJ*, 491, 381
- Reig, P., Fabregat, J., & Coe, M. J. 1997, *A&A*, 322, 193
- Shafter, A. W., Szkody, P., & Thorstensen, J. R. 1986, *ApJ*, 308, 765
- Taylor, A. R., & Gregory, P. C. 1982, *ApJ*, 255, 210
- Taylor, A. R., Kenny, H. T., Spencer, R. E., & Tzioumis, A. 1992, *ApJ*, 395, 268
- Wen, L., Levine, A. M., Corbet, R. H. D., & Bradt, H. V. 2006, *ApJS*, 163, 372
- Valdes, F., Gupta, R., Rose, J. A., Singh, H. P., & Bell, D. J. 2004, *ApJS*, 152, 251

Zamanov, R. K., & Martí, J. 2000, A&A, 358, L55

Zamanov, R. K., Martí, J., Paredes, J. M., Fabregat, J., Ribó, M., & Tarasov, A. E. 1999, A&A, 351, 543

Zamanov, R. K., Reig, P., Martí, J., Coe, M. J., Fabregat, J., Tomov, N. A., & Valchev, T. 2001, A&A, 367, 884

TABLE 1
RADIAL VELOCITY AND H α MEASUREMENTS

Date (HJD-2,400,000)	ϕ (TG)	V_r (km s $^{-1}$)	$(O - C)$ (km s $^{-1}$)	ΔV_{ISM} (km s $^{-1}$)	W_λ (\AA)	$V_r(W)$ (km s $^{-1}$)	$V_r(V)$ (km s $^{-1}$)	$V_r(R)$ (km s $^{-1}$)	$W_\lambda(V) /$ $W_\lambda(R)$	V/R	FWHM(V) (\AA)	FWHM(R) (\AA)
51053.860	0.122	-34.7	4.3	-1.2	-11.01	-8.5	-202.5	144.9	0.75	0.96	4.29	5.45
51053.881	0.123	-31.4	7.6	-0.7	-11.29	-10.1	-202.0	144.5	0.73	0.95	4.21	5.43
51055.855	0.198	-40.6	-9.2	1.6	-11.65	-16.2	-197.8	143.7	0.82	0.93	4.70	5.30
51055.877	0.199	-37.1	-5.9	0.5	-11.76	-18.5	-195.3	145.3	0.83	0.89	4.77	5.14
51055.941	0.201	-39.2	-8.2	2.1	-11.75	-17.2	-197.9	143.3	0.85	0.91	4.84	5.16
51056.902	0.237	-23.5	3.5	0.3	-11.29	-18.6	-196.3	148.7	0.88	0.89	5.12	5.16
51056.923	0.238	-32.7	-5.8	0.6	-11.36	-20.7	-197.4	149.0	0.86	0.88	5.05	5.19
51056.945	0.239	-21.8	5.0	0.4	-11.67	-19.2	-197.3	146.0	0.82	0.91	4.85	5.40
51057.880	0.274	-21.5	5.5	1.6	-11.82	-30.8	-201.2	149.1	0.91	0.90	5.37	5.33
51057.901	0.275	-12.7	14.4	-0.4	-11.21	-29.1	-196.0	148.4	0.87	0.89	5.13	5.26
51057.922	0.276	-16.6	10.7	-1.0	-11.60	-26.8	-195.7	149.2	0.87	0.90	5.20	5.36
51058.869	0.312	-38.4	1.0	0.5	-11.11	-33.5	-203.2	145.2	0.82	0.90	5.09	5.60
51058.892	0.312	-40.8	-1.0	1.6	-10.80	-32.1	-201.8	150.1	0.86	0.88	5.38	5.55
51058.913	0.313	-33.4	6.8	-1.6	-10.91	-33.5	-199.6	149.4	0.87	0.91	5.29	5.55
51061.882	0.425	-30.9 ^a	33.1	-2.0	-12.77	-37.8	-200.8	140.3	0.93	0.92	6.53	6.48
51061.903	0.426	-27.6 ^a	36.5	-0.9	-13.56	-41.9	-201.0	137.3	0.95	0.93	6.63	6.54
51061.924	0.427	-30.4 ^a	33.7	-1.9	-12.86	-39.3	-191.1	150.8	1.27	0.99	7.60	5.89
51065.882	0.576	-68.2	-5.7	1.0	-11.35	-29.1	-225.8	129.4	0.64	0.77	4.64	5.61
51065.903	0.577	-67.0	-4.4	-0.3	-11.30	-29.1	-226.2	130.6	0.63	0.77	4.66	5.65
51065.946	0.579	-67.1	-4.6	-0.6	-11.65	-29.2	-225.2	126.5	0.61	0.79	4.44	5.72
51066.756	0.609	-60.2	1.5	-0.9	-11.60	-13.7	-217.3	132.9	0.59	0.76	4.67	5.96
51066.778	0.610	-66.9	-5.2	1.0	-12.30	-22.1	-215.8	128.7	0.57	0.77	4.41	6.01
51066.800	0.611	-66.9	-5.2	-1.3	-12.24	-16.5	-214.4	129.8	0.57	0.78	4.43	6.01
51421.937	0.014	-49.0	-2.5	-0.2	-9.16	-23.0	-209.5	136.7	0.66	0.69	4.79	5.01
51425.943	0.165	-34.8	0.1	-3.6	-10.74	-15.2	-207.8	150.7	0.89	0.92	5.60	5.75
51425.964	0.166	-36.4	-1.5	-3.5	-10.72	-25.3	-209.9	135.6	0.74	0.82	4.95	5.50
51427.933	0.241	-44.8	-18.1	-1.3	-9.34	-5.8	-205.6	149.5	0.84	0.85	6.20	6.32
51428.882	0.276	-42.7	-15.4	6.8	-9.07	-24.3	-212.6	146.4	0.63	0.69	5.17	5.60
51428.903	0.277	-41.8	-14.4	-0.8	-9.46	-25.1	-214.2	139.7	0.60	0.70	4.84	5.64
51429.880	0.314	-43.4	-2.9	-1.2	-9.69	-38.7	-202.4	138.5	0.67	0.72	4.94	5.32
51429.901	0.315	-37.5	3.4	-3.4	-9.42	-39.4	-202.0	138.3	0.68	0.75	4.90	5.41
51464.828	0.633	-58.4	2.6	1.0	-12.35	12.8	-218.0	149.1	0.51	0.71	4.35	6.09
51464.850	0.634	-57.8	3.3	0.2	-12.29	15.5	-217.9	148.0	0.49	0.70	4.33	6.13
51464.930	0.637	-62.4	-1.5	-4.1	-12.28	14.7	-222.6	142.7	0.48	0.69	4.31	6.18
51465.890	0.673	-70.5	-10.6	-3.6	-13.29	22.4	-220.5	143.1	0.49	0.74	4.38	6.60
51465.911	0.674	-62.2	-2.4	-3.2	-13.37	22.1	-222.1	140.9	0.48	0.72	4.47	6.77
51466.840	0.709	-62.4	-3.6	-3.7	-12.00	11.7	-221.2	143.6	0.46	0.80	4.06	7.08
51466.861	0.710	-62.0	-3.2	-3.8	-12.16	14.3	-220.4	142.5	0.45	0.79	4.05	7.11
51466.884	0.711	-63.0	-4.2	-11.5	-12.26	9.7	-223.0	139.1	0.45	0.79	4.05	7.04
51467.899	0.749	-83.6 ^a	-26.1	-14.8	-1.11	51.6	-200.5	96.3	0.20	0.30	3.07	4.49
51467.920	0.750	-79.9 ^a	-22.4	-12.3	-0.92	81.2	-225.3	91.9	0.14	0.20	3.28	4.70
51468.862	0.785	-82.2 ^a	-25.9	-7.0	-1.31	49.2	-225.3	74.0	0.12	0.35	2.11	6.02
51468.883	0.786	-79.0 ^a	-22.7	-4.3	-1.11	-9.1	-246.5	78.9	0.11	0.36	1.55	5.36
51469.872	0.823	-79.9 ^a	-25.0	-11.3	-1.05	-4.2	-230.1	83.5	0.18	0.41	2.53	5.68

TABLE 1—*Continued*

Date (HJD−2,400,000)	ϕ (TG)	V_r (km s ^{−1})	($O - C$) (km s ^{−1})	ΔV_{ISM} (km s ^{−1})	W_λ (Å)	$V_r(W)$ (km s ^{−1})	$V_r(V)$ (km s ^{−1})	$V_r(R)$ (km s ^{−1})	$W_\lambda(V) /$ $W_\lambda(R)$	V/R	FWHM(V) (Å)	FWHM(R) (Å)
51469.893	0.824	−81.8 ^a	−26.9	−8.0	−1.57	−23.3	−226.9	86.9	0.13	0.31	2.52	5.95
51491.798	0.651	−63.5	−2.9	−5.3	−12.80	4.0	−220.5	145.4	0.52	0.84	4.39	7.05
51491.820	0.652	−62.2	−1.7	−4.0	−12.79	4.0	−222.4	144.6	0.52	0.84	4.39	7.13
51492.757	0.687	−58.0	1.4	0.1	−11.51	15.8	−221.3	152.9	0.51	0.86	4.44	7.43
51492.779	0.688	−56.4	3.1	0.5	−11.06	12.7	−224.6	152.6	0.52	0.86	4.45	7.35
51493.740	0.724	−62.6	−4.3	4.6	−10.53	14.6	−218.3	140.2	0.48	0.92	3.82	7.28
51493.761	0.725	−57.2	1.1	2.0	−10.90	14.6	−219.4	140.1	0.49	0.93	3.87	7.38
51494.752	0.762	−56.0	1.0	−2.5	−10.27	11.6	−211.5	142.8	0.48	0.78	4.21	6.87
51494.773	0.763	−56.4	0.6	0.8	−10.06	11.2	−213.0	141.8	0.48	0.79	4.17	6.84
51495.809	0.802	−52.6	3.1	−5.6	−10.72	−4.8	−212.9	138.4	0.64	0.76	4.92	5.84
51495.830	0.803	−52.8	2.8	−5.5	−10.63	−1.5	−211.4	137.1	0.62	0.79	4.67	5.92
51496.800	0.840	−54.1	0.3	−4.1	−10.00	−19.2	−212.5	138.5	0.67	0.75	5.12	5.77
51496.821	0.840	−49.4	5.0	−0.1	−10.08	−15.2	−209.6	138.0	0.67	0.77	5.09	5.84
51497.765	0.876	−60.2	−7.2	−1.3	−10.06	−14.4	−215.1	145.5	0.65	0.74	5.23	5.96
51497.786	0.877	−56.8	−3.9	−3.5	−10.23	−11.2	−216.8	146.5	0.64	0.75	5.23	6.14
51817.802	0.955	−62.0	−12.5	−0.4	−8.63	−23.8	−219.1	139.6	0.61	0.72	4.21	4.92
51817.850	0.957	−60.0	−10.6	−0.1	−8.53	−25.9	−218.1	138.7	0.62	0.72	4.18	4.87
51818.830	0.994	−58.5	−10.9	1.2	−8.85	−23.8	−221.4	140.5	0.65	0.71	4.30	4.73
51818.851	0.994	−58.7	−11.1	0.8	−8.29	−16.7	−221.7	142.0	0.63	0.71	4.23	4.74
51819.817	0.031	−53.2	−7.7	2.0	−8.87	−12.6	−216.3	142.6	0.60	0.79	4.35	5.68
51819.840	0.032	−51.9	−6.4	−0.4	−9.16	−13.6	−215.3	143.0	0.61	0.72	4.53	5.33
51820.827	0.069	−51.5	−8.4	2.9	−9.30	−23.2	−215.9	133.3	0.55	0.73	4.00	5.30
51821.770	0.105	−44.5	−4.0	−0.6	−9.51	−31.8	−212.4	131.4	0.66	0.86	4.00	5.19
51821.792	0.105	−45.0	−4.5	0.8	−9.41	−25.8	−213.9	135.7	0.64	0.86	3.98	5.29
51822.812	0.144	−38.1	−1.0	1.9	−9.91	−23.8	−212.5	136.0	0.68	0.91	4.04	5.38
51822.834	0.145	−39.6	−2.5	1.1	−9.73	−22.2	−211.8	136.7	0.69	0.93	4.00	5.38
51823.762	0.180	−40.5	−7.0	−0.1	−10.90	−35.1	−215.8	137.7	0.80	0.93	4.60	5.35
51823.783	0.181	−37.0	−3.7	2.0	−10.75	−36.0	−213.7	136.2	0.79	0.92	4.56	5.32
51824.765	0.218	−25.0	4.0	5.7	−10.59	−25.8	−204.2	147.4	0.76	0.89	4.61	5.37
51824.786	0.218	−28.1	0.8	3.4	−10.43	−26.5	−202.6	146.9	0.80	0.86	4.79	5.16
51830.779	0.445	−59.6	4.7	0.4	−10.44	−43.1	−221.7	121.9	0.61	0.76	4.60	5.78
51830.801	0.445	−61.4	3.0	1.4	−10.18	−39.5	−220.5	122.2	0.59	0.77	4.44	5.84
51889.762	0.671	−53.2	6.8	1.2	−9.43	−27.5	−219.8	132.1	0.72	1.09	4.02	6.05
51889.783	0.671	−50.8	9.2	−1.5	−9.73	−25.8	−220.3	133.3	0.71	1.09	3.96	6.04
51890.669	0.705	−31.9 ^a	27.0	−1.4	−9.76	−13.5	−216.9	145.8	0.74	1.13	4.03	6.14
51890.690	0.706	−38.9 ^a	20.0	0.2	−9.54	−14.2	−215.2	144.1	0.74	1.14	3.96	6.13
51892.658	0.780	−42.8	13.7	−0.9	−10.76	−7.3	−216.1	142.3	0.68	1.02	4.24	6.37
51892.682	0.781	−43.6	12.9	−1.7	−10.96	−10.3	−215.8	138.0	0.66	1.00	4.20	6.39
51893.686	0.819	−51.6	3.5	−2.4	−11.15	−1.1	−210.1	120.8	0.51	0.89	3.90	6.80
51893.707	0.820	−52.7	2.4	−0.4	−11.42	−5.2	−208.8	121.1	0.54	0.91	3.91	6.66
51894.684	0.856	−52.9	0.8	0.7	−9.31	−13.6	−208.2	128.4	0.58	0.84	4.02	5.86
51894.705	0.857	−53.1	0.6	−0.8	−9.35	−11.8	−206.7	130.5	0.59	0.83	4.08	5.80
51895.733	0.896	−51.5	0.6	0.7	−9.88	−11.8	−203.9	131.6	0.58	0.78	4.36	5.84
51895.754	0.897	−48.1	4.0	−0.9	−9.77	−11.0	−201.9	132.5	0.59	0.79	4.25	5.68

TABLE 1—*Continued*

Date (HJD−2,400,000)	ϕ (TG)	V_r (km s ^{−1})	$(O - C)$ (km s ^{−1})	ΔV_{ISM} (km s ^{−1})	W_λ (Å)	$V_r(W)$ (km s ^{−1})	$V_r(V)$ (km s ^{−1})	$V_r(R)$ (km s ^{−1})	$W_\lambda(V) /$ $W_\lambda(R)$	V/R	FWHM(V) (Å)	FWHM(R) (Å)
51896.706.....	0.933	−42.5	8.1	−0.4	−8.73	−13.5	−203.7	144.9	0.68	0.84	4.21	5.19
51896.727.....	0.934	−41.1	9.4	−1.0	−8.56	−9.2	−201.7	146.8	0.66	0.83	4.12	5.23
51897.707.....	0.971	−46.7	2.1	0.2	−8.02	−19.4	−206.4	140.4	0.66	0.89	3.77	5.08
51897.728.....	0.971	−43.1	5.7	−1.1	−7.97	−18.3	−206.7	139.0	0.67	0.90	3.83	5.11
51898.711.....	0.008	−42.6	4.3	−0.7	−8.24	−21.9	−207.4	143.1	0.77	0.92	4.23	5.04
51898.732.....	0.009	−45.5	1.2	−0.6	−8.28	−21.8	−206.7	144.4	0.79	0.91	4.34	5.00
51899.713.....	0.046	−31.9	12.7	0.2	−8.52	−19.2	−207.1	145.7	0.72	0.89	4.24	5.26
51899.734.....	0.047	−36.0	8.6	−0.1	−8.54	−16.0	−208.2	145.0	0.72	0.90	4.26	5.29
51900.708.....	0.084	−35.1	7.0	2.0	−9.23	−10.5	−200.3	137.5	0.68	0.90	4.21	5.52
51900.729.....	0.085	−36.3	5.7	1.0	−9.56	−12.5	−200.7	139.0	0.69	0.90	4.24	5.52
51901.693.....	0.121	−35.8	3.4	0.7	−9.18	−12.3	−200.1	134.4	0.72	0.92	4.23	5.36
51901.714.....	0.122	−35.6	3.4	1.3	−9.63	−11.9	−201.5	134.3	0.72	0.88	4.34	5.34

^aAssigned zero weight.

TABLE 2
ORBITAL ELEMENTS

Element	Hutchings & Crampton (1981)	Casares et al. (2005)	All Measures	Edited Set
P^a (d)	26.51	26.4960	26.4960	26.4960
T (HJD-2,400,000)	43559 ± 1	43372.9 ± 0.5	51057 ± 1	51058.6 ± 0.3
Periastron (ϕ (TG))	0.25 ± 0.04	0.23 ± 0.02	0.24 ± 0.04	0.301 ± 0.011
e	0.60 ± 0.13	0.72 ± 0.15	0.34 ± 0.08	0.55 ± 0.05
ω (deg)	46 ± 23	21 ± 13	15 ± 17	57 ± 9
K (km s $^{-1}$)	24 ± 6	23 ± 6	15.8 ± 1.4	19.3 ± 1.5
γ (km s $^{-1}$)	-57 ± 3	-40.2 ± 1.9	-49 ± 1	-51.0 ± 0.8
$f(m)$ (M_\odot)	0.019 ± 0.015	0.011 ± 0.012	0.009 ± 0.003	0.011 ± 0.003
$a_1 \sin i$ (R_\odot)	10 ± 3	8 ± 3	7.8 ± 0.7	8.4 ± 0.8
r.m.s. (km s $^{-1}$) ...	15.6	8.5	10.4	7.5

^aFixed.

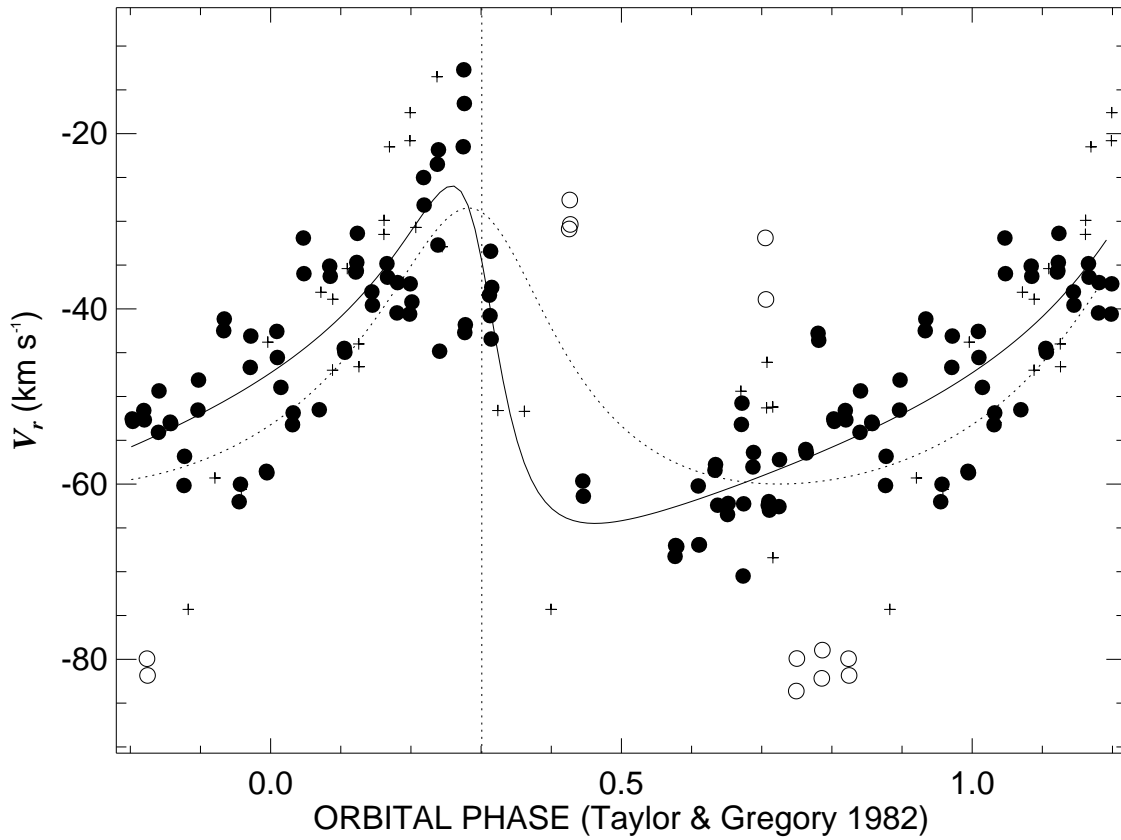


Fig. 1.— Calculated radial velocity curve (*solid line*) for LS I +61 303. The measured radial velocities are shown as filled circles. Open circles mark the measurements that were assigned zero weight, and plus signs indicate the measurements from Casares et al. (2005). The curved dotted line shows the orbital solution that results when the discrepant measurements are included in the fit. The vertical dotted line indicates periastron phase.

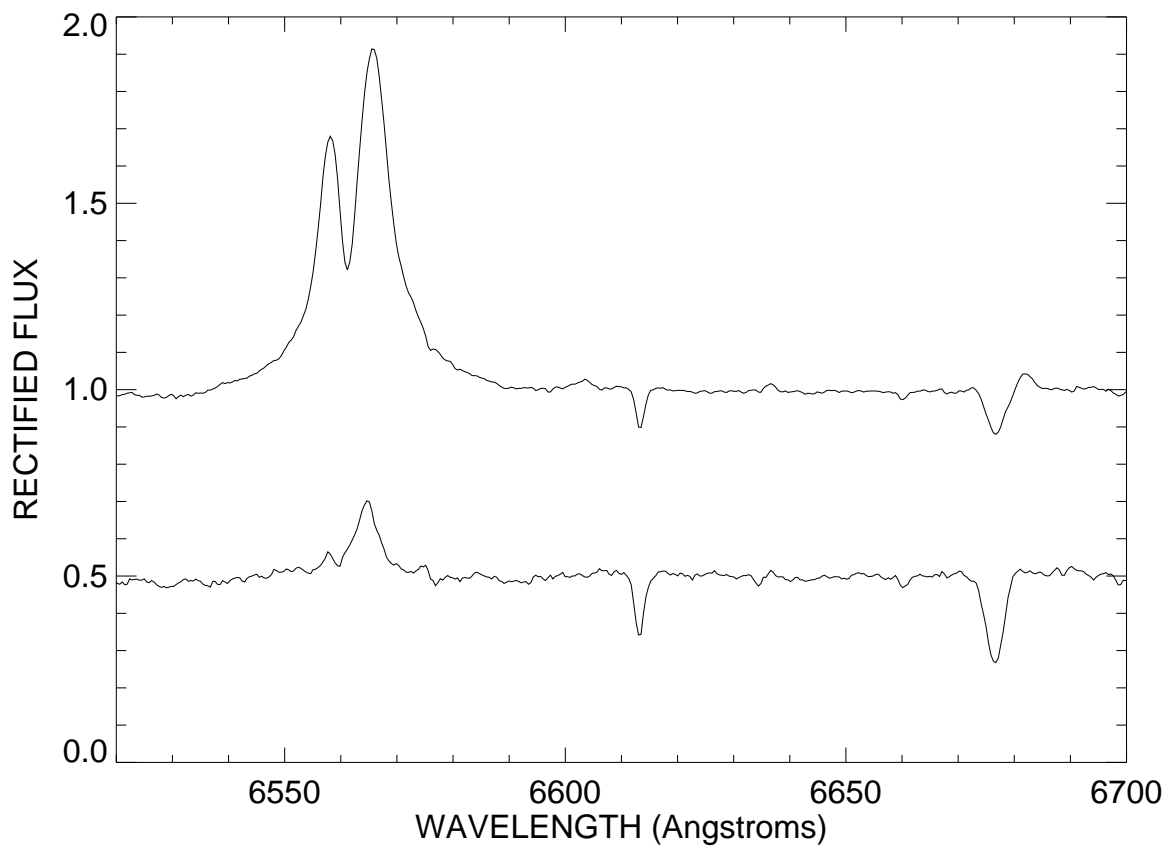


Fig. 2.— Average spectra of LS I +61 303 from 1999 October. The top plot shows the average from the first three nights when the $H\alpha$ emission strength was normal, while the bottom plot (offset by -0.5 in rectified flux for clarity) shows the average from the next three nights when the emission strength plummeted. The other spectral features shown are the interstellar 6613 \AA line and He I $\lambda 6678$.

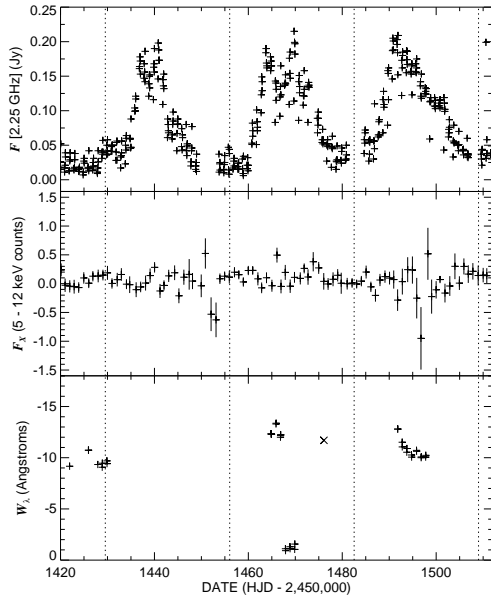


Fig. 3.— The time variations in radio flux (*top panel*), X-ray emission (*middle panel*), and H α emission equivalent width (*lower panel*) around the time of the H α emission decline. The X symbol in the lower plot represents an equivalent width measurement from Liu & Yan (2005). The dotted lines indicate times of periastron.

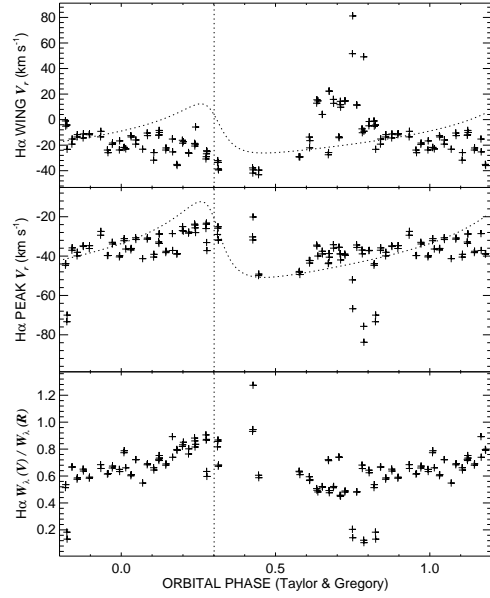


Fig. 4.— The orbital phase variations in the H α wing radial velocity (*top*), the mean H α peak radial velocity (*middle*), and the ratio of the equivalent widths of the *V* and *R* components (*bottom*). The curved dotted lines in the upper two panels show the orbital radial velocity curve translated to the mean velocity of the sample in each case. The vertical dotted line indicates periastron phase.

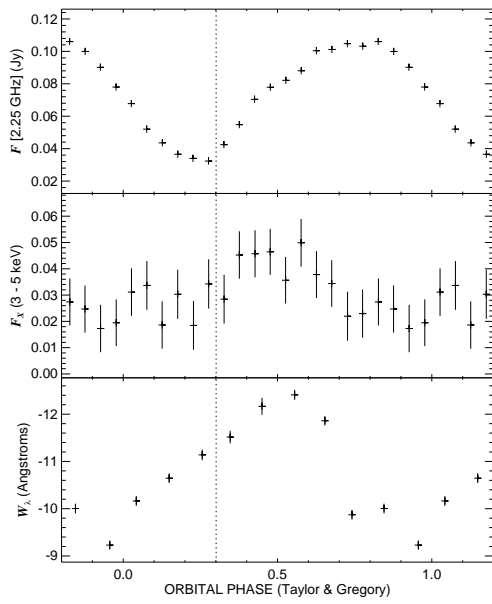


Fig. 5.— The variations in radio flux (*top panel*), X-ray emission (*middle panel*), and H α emission equivalent width (*lower panel*) binned and plotted as a function of orbital phase. The vertical bars through each point express the standard deviation of the mean in the phase bin. The vertical dotted line indicates periastron phase.

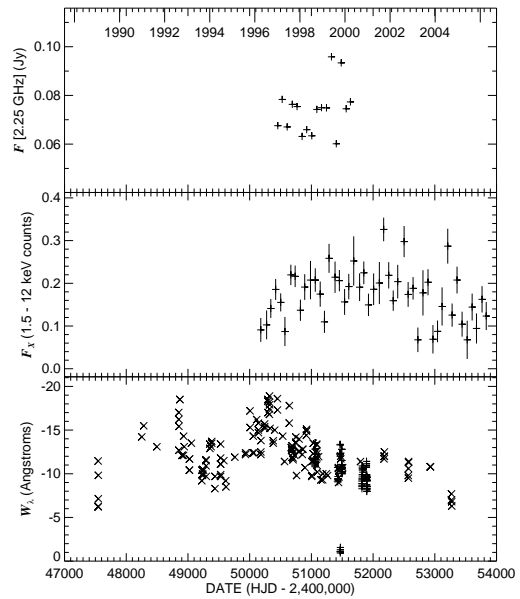


Fig. 6.— The time variations in radio flux (*top panel*), X-ray emission (*middle panel*), and H α emission equivalent width (*lower panel*) over the period of active observation. The values in the upper two panels represent binned averages over time bins of three orbital periods. The X symbols in the lower plot represent other published equivalent width measurements.

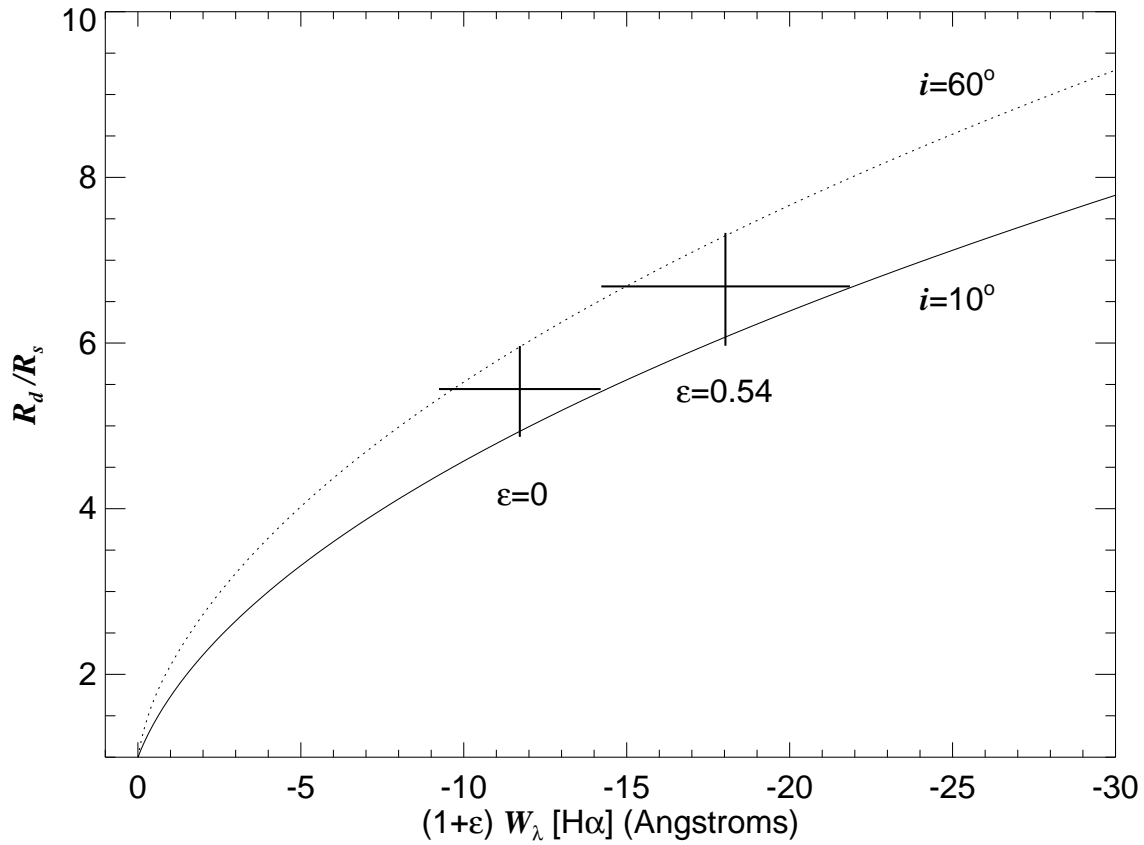


Fig. 7.— The predicted relationship between H α equivalent width (referenced to the stellar continuum level) and disk radius for two values of disk inclination. The two crosses indicate the observed mean equivalent width with no adjustment for the disk continuum flux ($\epsilon = 0$) and with the optical disk flux contribution suggested by Casares et al. (2005) ($\epsilon = 0.54$).